10 Electromagnetic Calorimeter

10.1 Overview

Electromagnetic calorimeters (EC) are used in both PVDIS and SIDIS experiments to measure the energy deposition of electrons and hadrons, and to provide particle identification (PID). For electron detection, the dominant background comes from electro- and photo-produced pions. There are three calorimeters for the SoLID experiments: the PVDIS experiment uses a forward angle calorimeter (FAEC), and the SIDIS experiments use a forward angle calorimeter (FAEC) and a large angle calorimeter (LAEC). The desired performance is summarized in Table 7. The EC geometry in Table 8. Please note that EC geometrical coverage are a little larger than other detectors because the performance at edges of EC are degraded due to EM shower spreading. The total coverage area of SIDIS FAEC and LAEC are less than that of PVDIS FAEC. The plan is to share modules between the two configurations.

	Desired performance
π^- rejection	$\gtrsim$[50:1] for above Cerenkov threshold
e^- efficiency	$\gtrsim$95%
Energy resolution	$< 10\%/\sqrt{E}$
Radiation resistance	$\gtrsim$400 kRad
Position resolution	$\lesssim$1 cm

Table 7: Overview of the SoLID calorimeter desired performance

	PVDIS FAEC	SIDIS FAEC	SIDIS LAEC
z (cm)	(320, 380)	(415, 475)	(-65, -5)
Polar angle (degree)	(22,35)	(7.5,14.85)	(16.3, 24)
Azimuthal angle	Full coverage		
Radius (cm)	(110, 265)	(98, 230)	(83, 140)
Coverage area (m^2)	18.3	13.6	4.0

Table 8: Geometrical coverage for the SoLID electromagnetic calorimeters. The z direction is along the electron beam and the origin is at the solenoid center. The range of various dimensions are shown.

Design of the SoLID EC is determined by both the physics goal and the expected running conditions. The design is challenging due to our unique constraints including high radiation background ($\approx$400 kRad, as in Table 7), strong magnetic field (1.5 T on SIDIS LAEC), large coverage area, and the budget. These factors prevent the use of many traditional calorimeter technologies, including NaI (Tl), CSI, BGO and lead-glass because of the low radiation resistance; $PbWO_4$, LSO and PbF_2 because of their high cost; and lead/scintillator fiber calorimeter because of the high cost and the large amount of light readout required.

Due to the PID requirement, it is necessary to segment the EC into a preshower and a shower detector. The following design that meets the experimental requirements was chosen: the shower calorimeter modules are based on the so-called Shashlyk design [1] – a sampling-type design consists of alternating layers of scintillator and lead (as an absorber); the preshower detector is made of a layer of lead as a passive radiator followed by scintillator pads [2, 3]. Details of the design is summarized in Tables 9 and 10.

Type	passive radiator + sensitive layer
passive radiator	$2X_0$, Pb
Sensitive layer	2 cm, plastic scintillator 100 cm^2 hexagon tile
Light transportation	WLS fiber embedded in scintillator

Table 9: SoLID electromagnetic calorimeter, preshower design.

Type		Shashlyk sampling calorimeter
Each layer	Absorber	Pb, 0.5 mm
	Scintillator	STYRON 637 plastic scintillator, 1.5 mm
	Gap	Paper, 0.12 mm $\times$ 2 sheets per scintillator layer
	Radiation Length	$0.093X_0$
Overall	Radiation length (X_0)	24 cm
	Molire radius	5 cm
	Length	18 X_0, 43.4 cm
	Layer count	194
	Lateral granularity	100 cm^2 hexagon
	Light transportation	WLS fiber, penetrating layers longitudinally

Table 10: SoLID electromagnetic calorimeter, shower design.

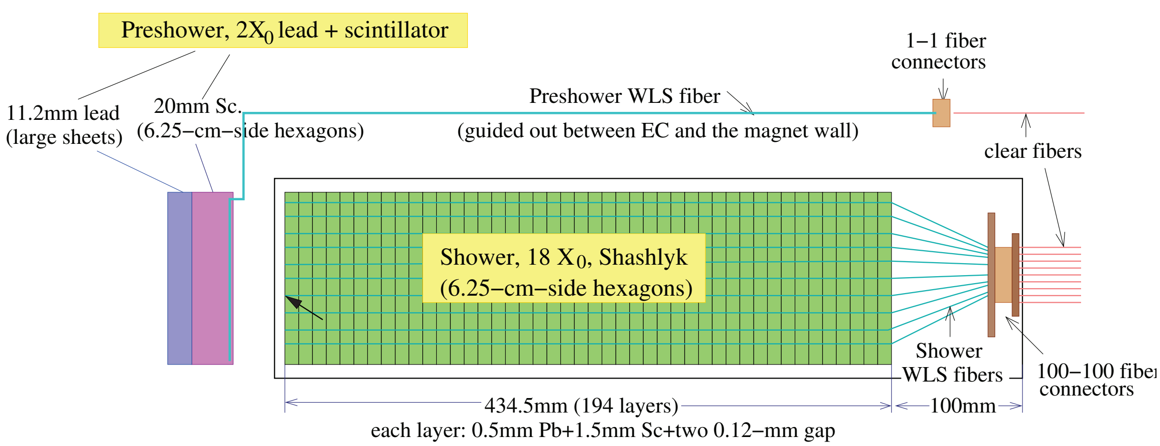

Figure 84: Design diagram of the SoLID electromagnetic calorimeter module. Spacing between the preshower and the shower detectors, and the spacing between the shower module and the 100-100 fiber connectors, need to be kept as small as possible yet still allow safe routing of the WLS fibers and positioning of the support structure.

The structure of both the preshower and the shower detector are illustrated in Fig. 84. In the experiment, particles incident close to perpendicular to the scintillator-lead layers. Scintillation light is absorbed, re-emitted and transported to the photon detector by wave-length shifting (WLS) optical fibers penetrating through the shower modules longitudinally, along the impact particle direction. The cross sectional area of the shower modules was optimized to be 100 cm^2 (see Section 10.2.3), with a hexagon shape determined for the convenience of the support structure design. The scintillator tile of preshower modules has the same 100 cm^2 hexagon shape to match the shower modules, which maximizes PID efficiencies, facilitates the design, and allows fast switch-over between SIDIS and PVDIS. The lead absorber of the preshower can be made of large sheets.

The Institute for High Energy Physics (IHEP) of Russia has extensive experience in the R&D and mass production of Shashlyk type calorimeters. They were consulted and provided inputs to the design of the SoLID EC. Currently they are expected to be the primary manufacturer for the SoLID EC.

Geant4-based simulations are used to study the performance and optimize the design of the key specifications while minimizing the cost. Figure 85 shows the simulated shower of a 3 GeV electron incident on the PVDIS EC. In the following we will present details of the shower and the

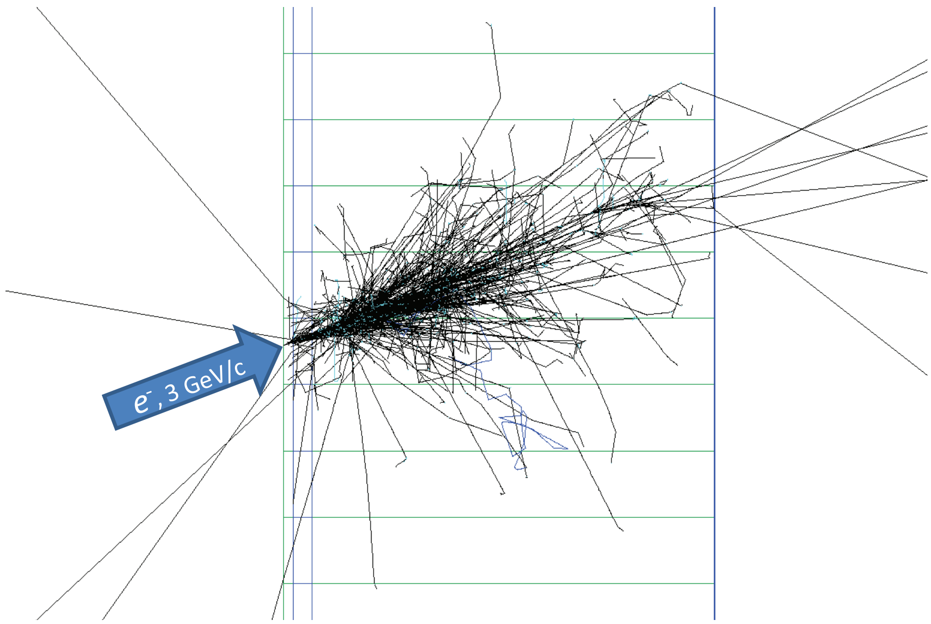

Figure 85: GEANT4 simulation of the shower generated by a 3-GeV electron incident on the PVDIS calorimeter. The black and green tracks are secondary photons and electrons respectively. The green horizontal lines are edges of calorimeter modules. The first two layers of materials are the preshower detector, consisting of $2X_0$ of lead and 2 cm thick of scintillator.

preshower design, general layout and the support system, light readout, expected radiation dose, PID and trigger performance, and a cost estimate.

10.2 Shower Detector Design Considerations

10.2.1 Total Length of the Calorimeter

The overall length of calorimeter should be long enough to enclose most of the electromagnetic shower and short enough to maximize the difference in energy deposition between electrons and pions. The fraction of energy leak out for electron showers, averaged inside the acceptance of the SIDIS-Forward calorimeter, was studied for different total lengths of calorimeter. As shown in Fig.86, a total length of 20 radiation lengths was found to be a good balance. Considering the 2-radiation-length thickness of preshower, this leads to a shower detector length of 18 radiation lengths or 43.4 cm.

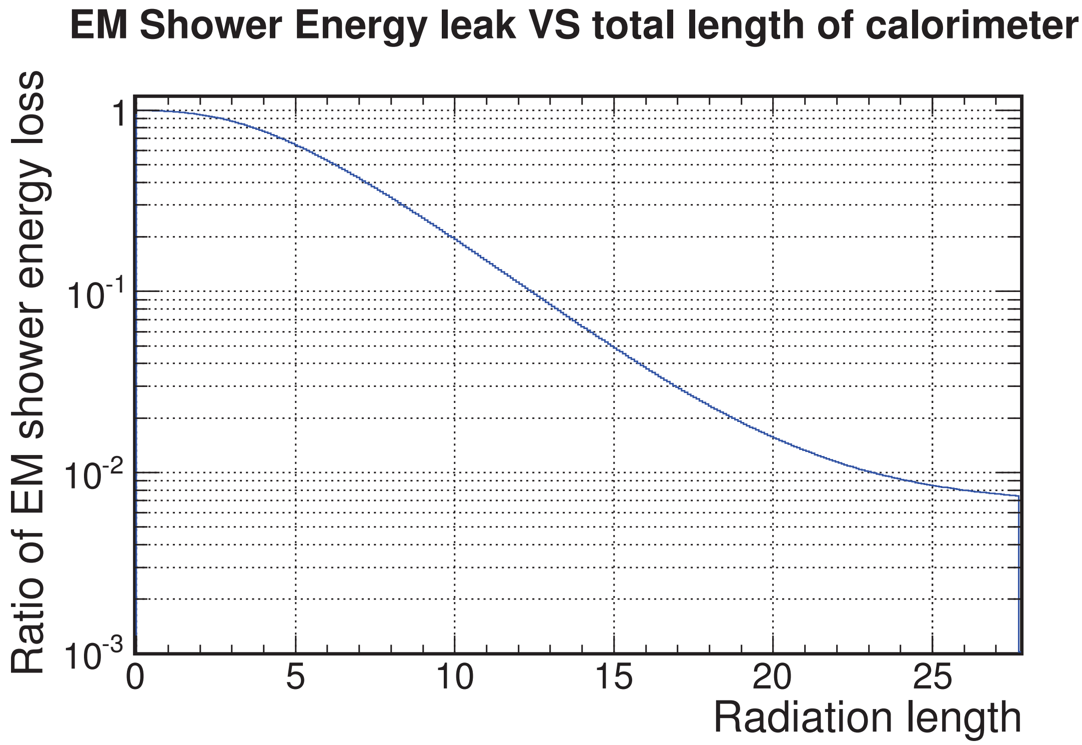

Figure 86: Fractional energy leak for an average SIDIS-Forward electron shower vs. different total length of the calorimeter.

10.2.2 Sampling Ratio of the Shower Detector

Each layer of the shower module consists of a 1.5 mm-thick scintillator plate and a 0.5-mm absorber plate made of lead. The Pb absorber thickness of 0.5 mm or less is favored to provide a fine sampling and therefore better energy resolution. The thickness of the scintillator plate should be thin enough to ensure fine longitudinal sampling, while thick enough to reduce light attenuation on the lateral direction. A thickness of 1.5 mm was chosen following the experience of previous Shashlyk designs used by the KOPIO experiment [1, 4], the PANDA experiment [5], and the COMPASS-II experiment. The COMPASS module is shown in Fig. 87. A gap of 120 μm is kept between each lead and scintillator plates to accommodate a sheet of paper, which reduce the loss of scintillation light.

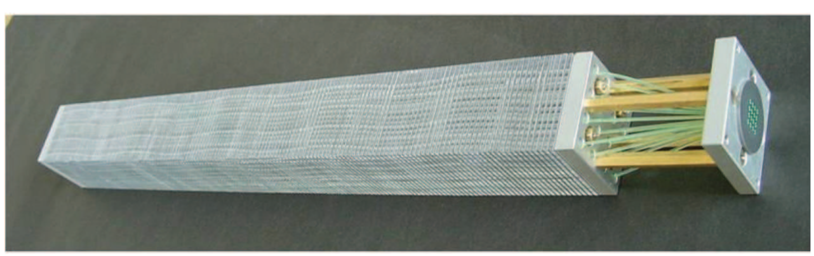

Figure 87: COMPASS II Shashlyk calorimeter module.

Figure 88 shows the energy resolution using the chosen configuration of 1.5 mm scintillator and 0.5 mm lead. A resolution of about $4\%/\sqrt{E}$ is achieved.

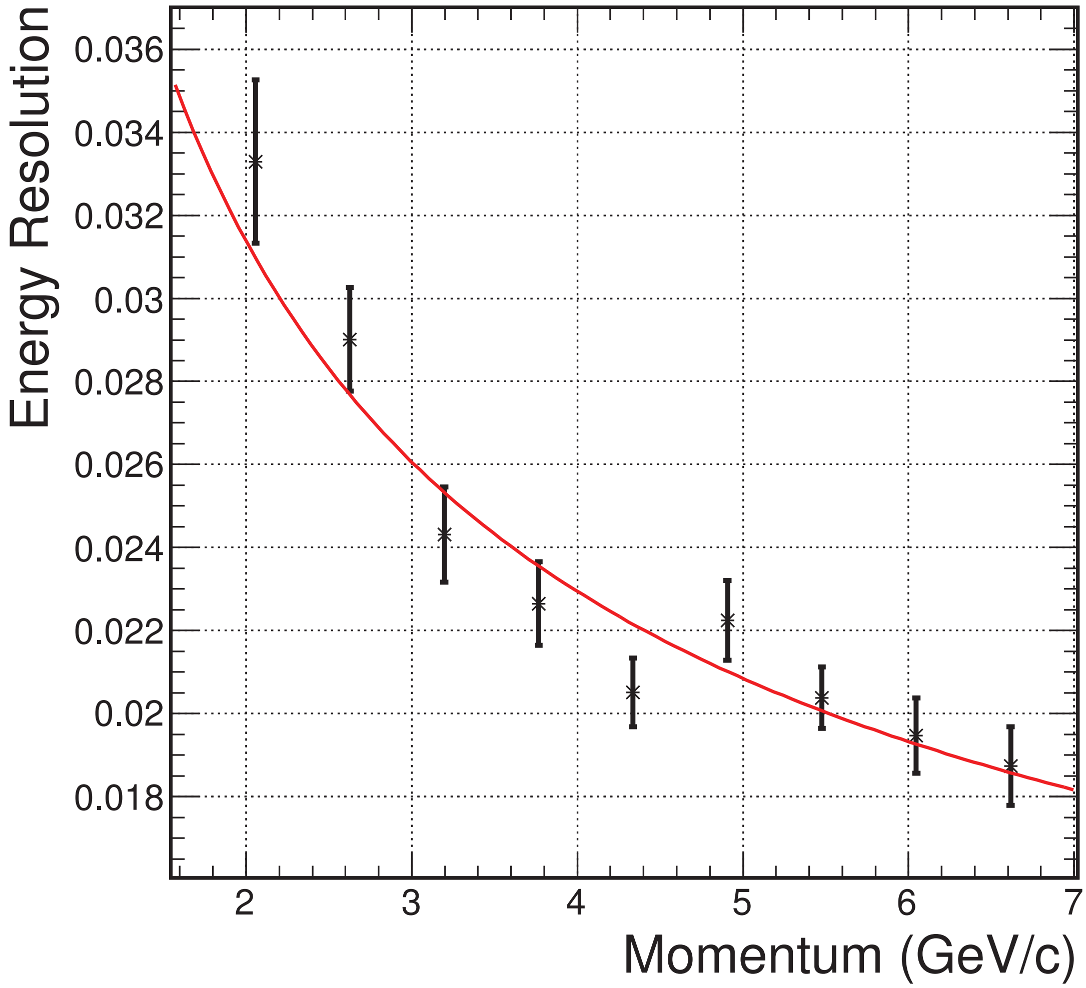

Figure 88: Energy resolution of the SoLID calorimeter (preshower + shower).

10.2.3 Lateral Size of the Calorimeter Module

A smaller lateral size for calorimeter modules leads to a better position and lower background. However, it will also increase the total number of modules and channels readouts, therefore higher overall cost. The study shows that a lateral size of about 100 cm^2 will provide a good balance between position resolution, background and the overall cost as shown in Fig. 89. A hexagon lateral shape is favored by the layout and the support design.

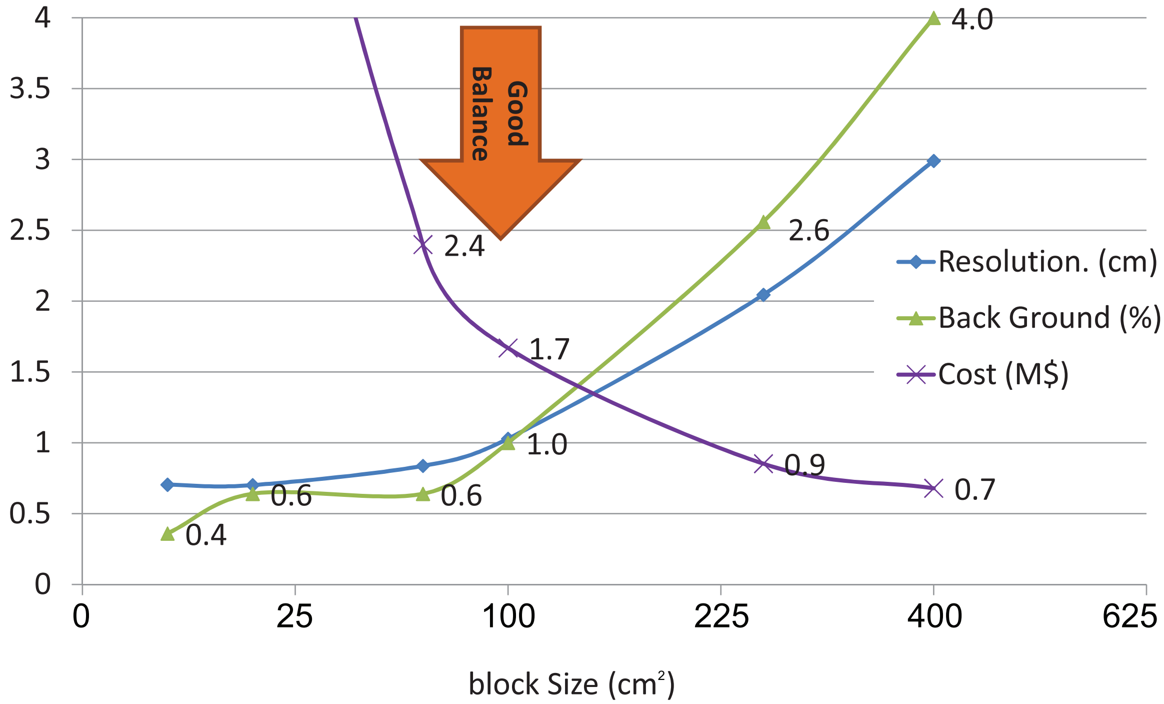

Figure 89: Position resolution and background level from simulation and the cost of the shower detector vs. lateral block size (1D or square root of the cross-sectional area) of the module.

10.3 Preshower Detector

Segmenting the EC longitudinally into a preshower and a shower part is essential to reaching the required pion rejection. Two designs were considered for the preshower detector: a full Shashlyk-type design that is optically isolated from the shower detector, and a passive radiator/scintillator pad design as used in the HERMES [2] and LHCb [3] experiments. Comparing to a Shashlyk-type preshower, the passive radiator/scintillator pad design have several advantages including increased radiation hardness, simplicity in construction, and fewer WLS fibers to readout. For a passive radiator of $2X_0$, the impact to overall energy resolution is less than $0.5\%/\sqrt{E}$ for electrons with momentum larger than 2 GeV$/c$. Therefore, the passive radiator/scintillator pad design was adopted for the preshower detector. Details of the design are as follows:

- The thickness of preshower radiator was determined by optimizing the overall pion rejection at the desired electron efficiency. As shown in Fig. 90a, the preshower-alone pion rejection improves as the radiator thickens up to $3.5X_0$ due to immediate development of the electromagnetic shower. However, the impact to the overall energy resolution degrades with increased thickness of the absorber. A thickness of $2X_0$ for the radiator was found to be an optimal choice for the SoLID application.

- The scintillator and readout design is similar to that of the LHCb experiment [3], as illustrated in Fig. 91. A single WLS fiber is embedded in one 2 cm-thick scintillator pad. It absorbs, re-emitted and conducts the photons for readouts.

With the above configuration, the relation between pion rejection and electron efficiency for preshower alone can be plotted as a function of scintillator energy cuts, as shown in Fig. 90c. One can see a pion rejection of better than $5:1$ can be achieved at an electron efficiency of $> 94\%$.

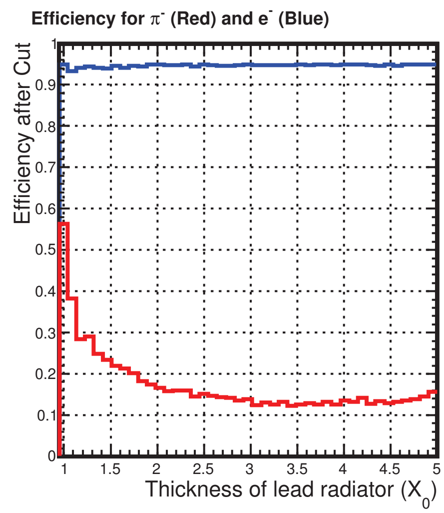

(a)

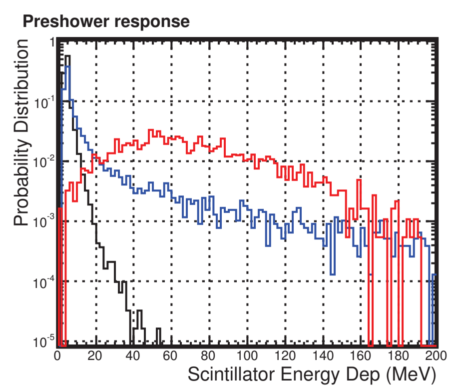

(b)

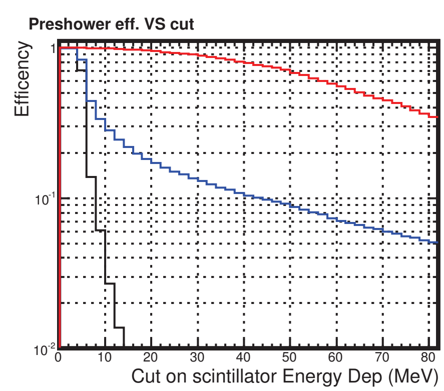

(c)

Figure 90: Simulated performance for the preshower detector: (a) $1/(\pi^-$ rejection$)$ (red curve) at a 95% electron efficiency (blue curve) vs. different thickness of the lead radiator. (b) Energy deposition in the scintillator (left) and (c) detector efficiency vs. energy deposition cut (right), for electrons (red), π^- (blue) and μ^- (black), for a preshower consisting of $2X_0$ of lead radiator and 2 cm of scintillator.

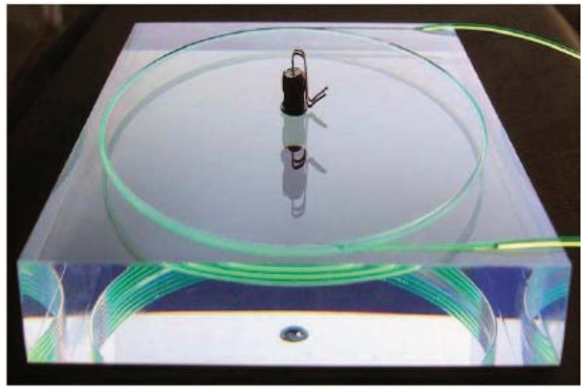

Figure 91: Reading out photons in the scintillator using a single wavelength shifting fiber as used in the LHCb experiment [3]. The WLS fiber is embedded in a circular grove cut by a diamond cutter.

10.4 Layout and Support

The total areas of PVDIS EC and SIDIS ECs coverages are almost the same. The modules will be re-arranged between the two configurations, where modules from PVDIS FAEC will be split and re-arranged into SIDIS FAEC and LAEC. The SIDIS EC layout must preserve the 2-fold rotation symmetry in the spectrometer. The design layout that meets these requirements as shown in Fig.92. The forward angle EC support is shared by PVDIS FAEC and SIDIS FAEC and SIDIS LAEC has a similar but separate support.

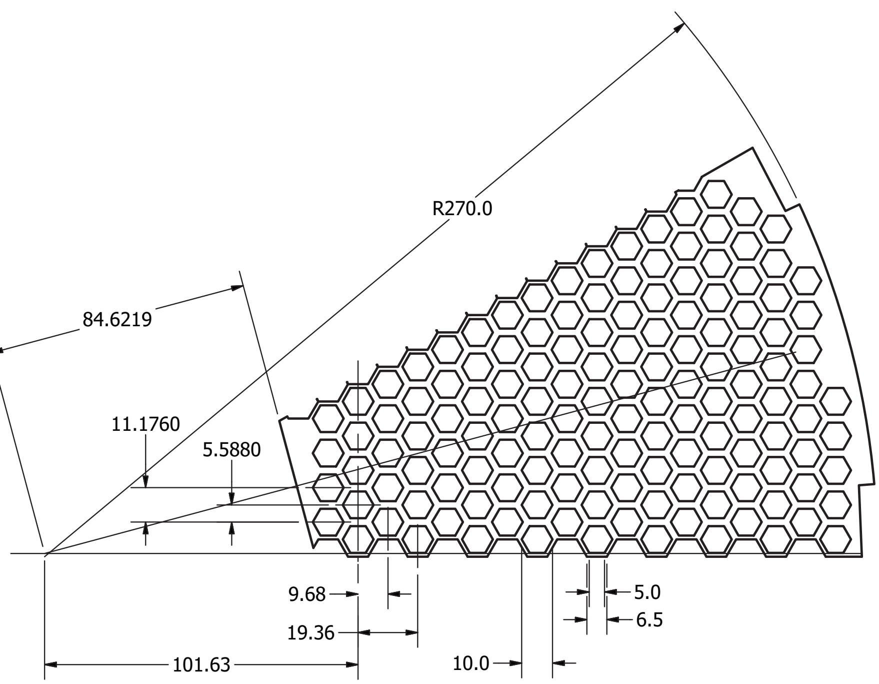

Figure 92: Layout of the hexagon-shaped modules with their support for a 30-degree wedge of the FAEC.

The scintillator tiles of preshower modules will be mounted on a 2-cm thick aluminum plate.

For shower modules, the lead and the scintillator layers in each Shashlyk module are held together by four stainless steel rods penetrating longitudinally through the module. These rods are supported by two aluminum plate-like structures, one between preshower and shower, and one 4-cm thick plate behind the Shower. The thickness of the first aluminum plate must be minimized to reduce the impact on the PID and trigger capability. The current design is to have this supporting plate of 1 cm.

10.5 Light Readout

The blue light from scintillators is converted into green light by WLS fibers penetrating through the modules. To efficiently collect scintillation light, a total of 100 1-mm-diameter WLS fibers are needed for each shower module, arranged along the direction of the particle trajectory. For preshower modules, only one 1-mm-diameter WLS fiber is needed due to the small thickness of their scintillators. WLS fibers of shower modules will be guided directly towards the back of EC, while WLS fibers of preshower modules will be routed using the space between preshower and shower, to the space between EC and the solenoid wall. To avoid light loss over long distances, WLS fibers will be connected to clear fibers using one-to-one connectors for readout by PMTs. Figure 93 shows a custom design of the fiber connector for shower modules. For preshower modules we will use commercially-available single-fiber connectors.

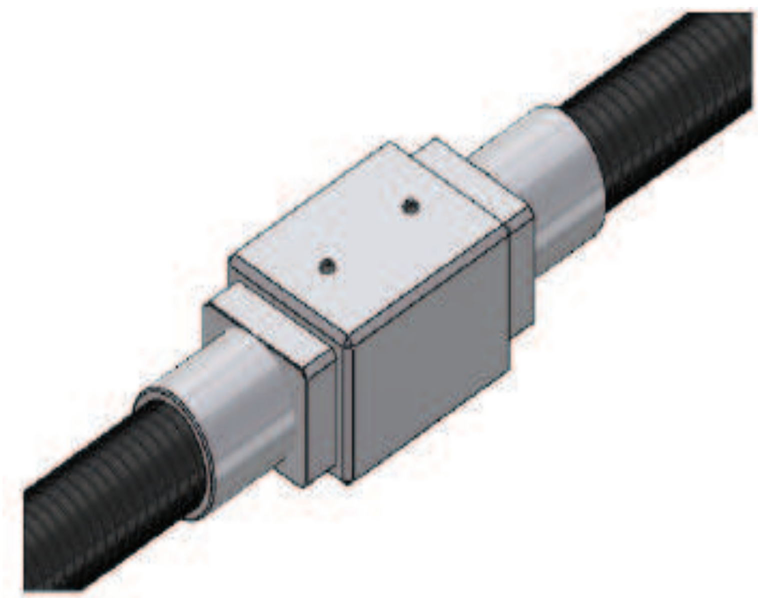

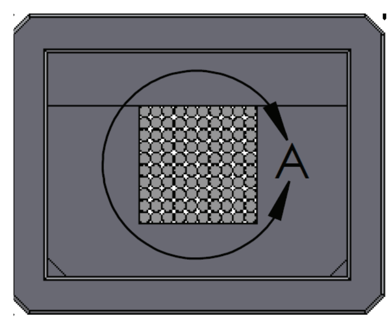

Figure 93: A custom design for the shower module fiber connector. Each connector can be used to link 100 WLS to 100 clear fibers.

The Bicron BCF91a WLS fiber is chosen as a balance between the required radiation hardness and the cost. The magnetic field reaches about 1.5 T behind SIDIS LAEC and a few hundred Gauss behind both PVDIS and SIDIS FAEC. Field-insensitive photon sensors are in general expensive and less radiation-hard compared to PMTs. Therefore, the default design is to use PMTs. One PMT is needed for each shower module (100 fibers) and each preshower module (1 fiber). To reduce cost for readout, multi-anode PMTs (MAPMTs) are being considered for preshower modules and gainmatching between MAPMT channels might be posisble using the FADC. Further R&D of MAPMT is needed and it is not yet adopted as this document is written.

There are also field insensitive photon sensors that can be used for readout. SiPM has enough gain (10^6) for sampling calorimeters, but its dark rate is prone to neutron background. We are still evaluating the neutron background at the calorimeters and the choice of SiPM as direct readout without the need of fiber connectors and clear fibers.

10.6 Radiation Effect

EC for the SoLID spectrometer are designed for high luminosity experiments. The expected luminosity and run time are 169 PAC-days at $10^{39} N \cdot \mathrm{cm}^{-2}\mathrm{s}^{-1}$ in the PVDIS configuration, 245 PAC-days at $10^{37} N \cdot \mathrm{cm}^{-2}\mathrm{s}^{-1}$ for the SIDIS experiments and 60 PAC-days for the J/Ψ experiment. In the current design, the maximum radiation dose on the active material – scintillator and WLS fibers – in the calorimeter is significantly reduced by the use of the $2X_0$ lead plate in the Preshower, and the lead blocks described in Section 6.

The radiation dose inside calorimeter was simulated using GEANT4 based simulations considering a wide range of energy and species for the background particles. The dose rates for the active material (scintillators and fibers) are shown in Figure 94 and Figure 95. The highest radiation region is at the front part of the calorimeter, including the preshower scintillator pad and the front scintillators of the Shashlyk calorimeter modules. The maximum integrated radiation level for the active material reaches 100 kRad for the PVDIS experiment and 20 kRad in the SIDIS and J/Ψ experiments, which leads to a total radiation dose of less than 200 kRad for all approved experiments. This dose level can be safely handled by the choice of scintillator and WLS fibers.

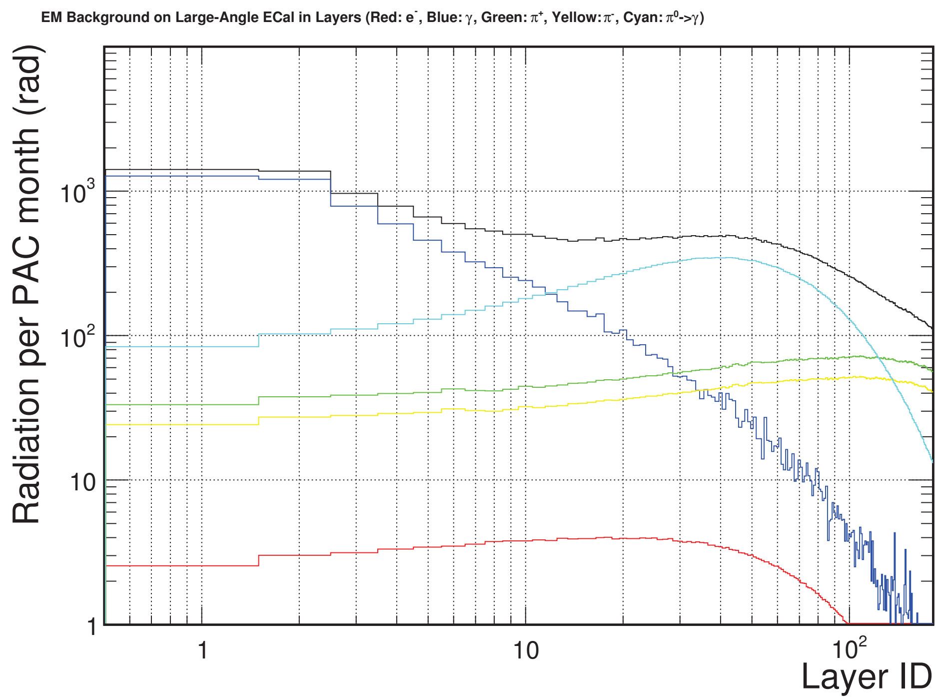

(a) SIDIS large-angle calorimeter

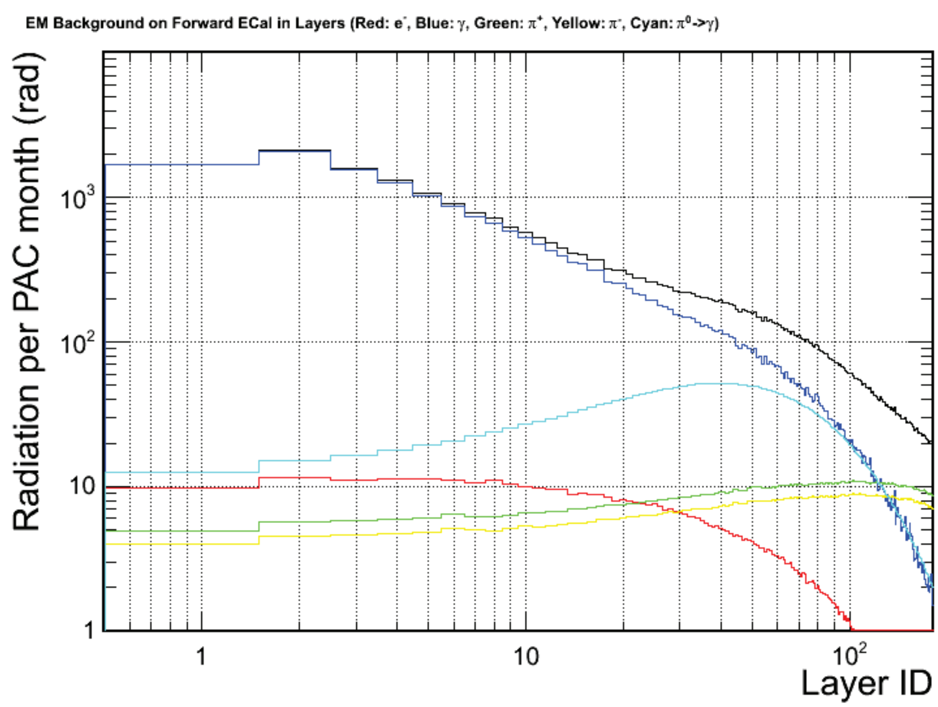

(b) SIDIS forward-angle calorimeter

Figure 94: SIDIS Radiation dose rates in each layer of the scintillator tiles in the calorimeter. Layer ID 1 is the preshower scintillator. The rest of IDs are assigned for each scintillator layer in the Shashlyk calorimeter in the order of increasing z. The color code stands for different contributions of various particle species at the front surface of the preshower: electrons (red), photons (blue), EM total (magenta), π^+ (green), π^- (yellow). The overall dose is shown by the black curve.

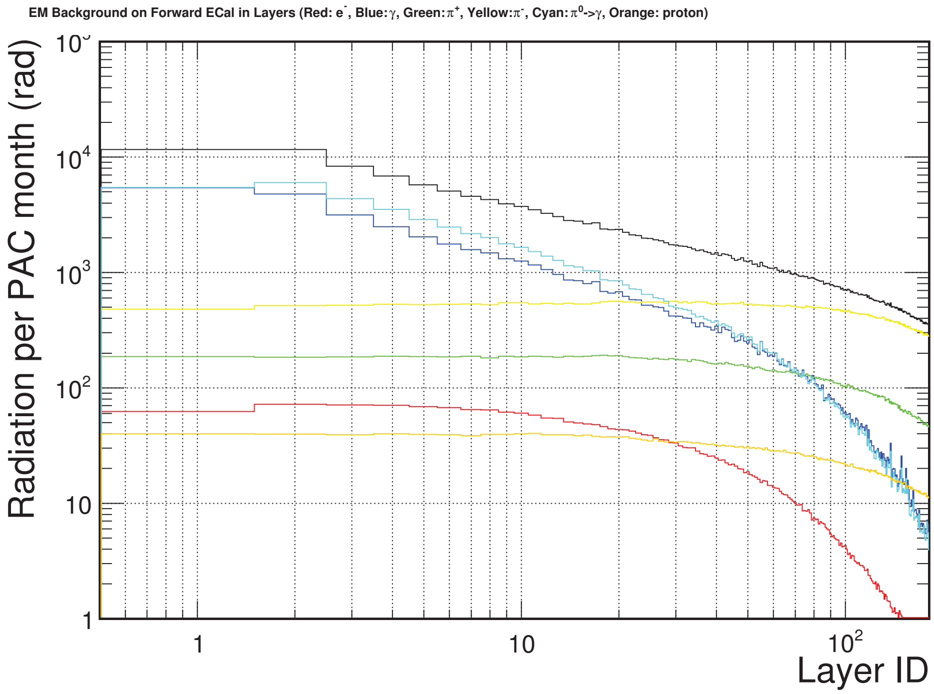

(a) PVDIS calorimeter in higher-photon flux region

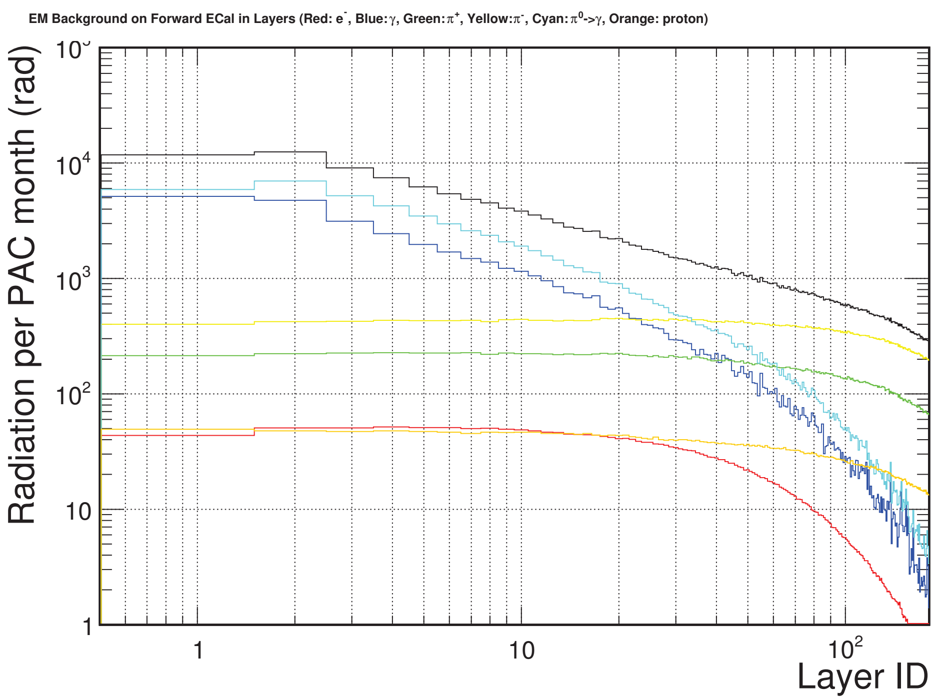

(b) PVDIS calorimeter in lower-photon flux region

Figure 95: PVDIS Radiation dose rate in each layer of the scintillator tiles in the calorimeter. Layer ID 1 is the preshower scintillator. The rest of IDs are assigned for each scintillator layer in the Shashlyk calorimeter in the order of increasing z. The color code stands for different contributions of various particle species at the front surface of the preshower: electrons (red), photons (blue), EM total (magenta), π^+ (green), π^- (yellow). The overall dose is shown by the black curve.

10.7 Performance

The EC system plays multiple roles in the SoLID spectrometer. Its performance was evaluated in the GEANT4 based simulation and discussed in this section, including PID performance, trigger capability and shower position resolution. A realistic background simulation was setup to evaluate the calorimeter considering a wide range of species and momenta of the background particles.

10.7.1 Intrinsic Electron-pion separation

As a baseline, the PID performance was first evaluated without the background. The primary track is propagated through the SoLID magnetic field in GEANT4, then enters the calorimeter. A local cluster which consists of the central calorimeter module and six neighboring hexagon-shaped modules is formed. With a multidimensional cut of the preshower and shower response within the cluster (see Sec. 10.8), the overall pion rejection averaged over the acceptance of each calorimeter is shown in Fig. 96. A $100 : 1$ pion rejection at 95% electron efficiency is achieved for momentum bins of $p > 2$ GeV/c. A better than $50 : 1$ pion rejection at 90% electron efficiency is obtained for the lowest momentum bin ($1 < p < 2$ GeV/c), which is only needed for the SIDIS forward calorimeter.

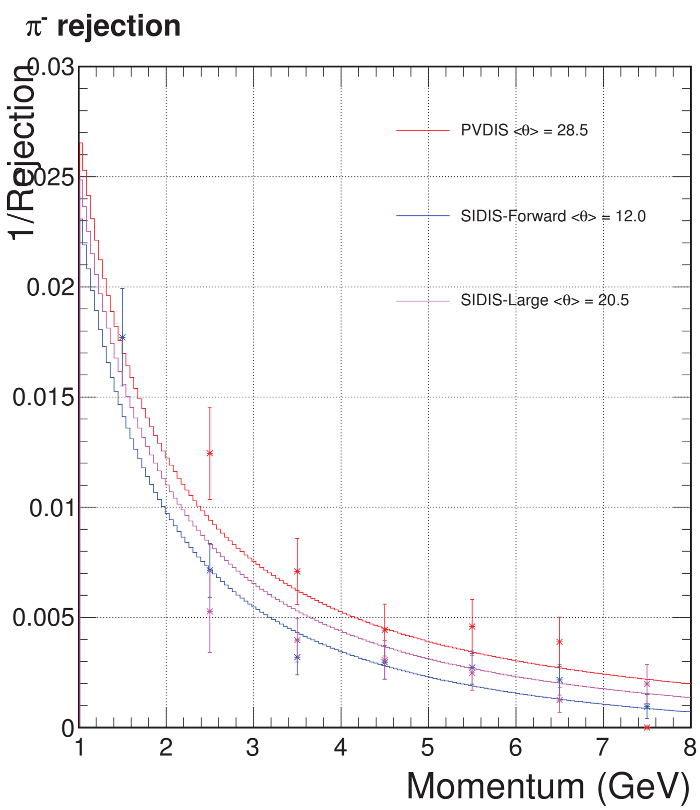

Figure 96: π^- efficiency (1/rejection). A constant 95% electron detector efficiency is maintained for $p > 2$ GeV/c. A 90% electron efficiency is maintained for the lowest momentum bin $1 < p < 2$ GeV/c, which is only required for the SIDIS forward calorimeter. The average track polar angle θ is different for the three calorimeter configurations, which leads to slight differences in the pion rejection curves.

10.7.2 PID performance under realistic background simulation

For a large intensity device, background particles and their influence on the calorimeter performance have to be considered. A full background simulation was implemented to study calorimeter performance. The background simulation procedure is as follows:

1. Particles are generated at the target including photons and electrons from the low energy EM processes (based on physics in GEANT4), DIS electrons (based on CTEQ6 PDF), and hadrons (based on Wiser fit);

2. Particles are propagated through a SoLID GEANT4 simulation to the front surface of calorimeter;

3. The EC response is simulated for a wide range of background particles – electrons, photons, pions, and protons – within the momentum range 10 keV$< p <$11 GeV A statistical model is used for the correlation between Preshower and Shower responses;

4. The background contribution to each event is produced by combining the background rate at the EC front surface and the EC response described above for a region of interest on the calorimeter, usually defined by a radius-azimuthal angular bin. A conservative 30 ns coincidental window between background particles and the primary event is assumed.

5. The background contribution is embedded into the raw signal from the simulated primary particles (high energy electrons and pions). The background-embedded data are then analyzed as raw ADC signals. The energy response is calibrated and PID and trigger performance are analyzed.

Typically, background rate is the highest in the inner radius region and drops by approximately one order of magnitude in the outer radius region. Figure 97 shows the EC performance for the SIDIS configuration in the inner radius region. For SIDIS experiments, effects from background particles are visible but not significant: for large-angle EC, the pion rejection remains better than 100:1 for all momentum bins; for forward-angle EC, there is no noticeable change in the PID performance other than for the lowest momentum bin $1 < p < 2$ GeV$/c$ where the pion rejection is a half of the no-background case. However, the Cherenkov detector provides high PID performance in the low momentum range and the overall pion rejection is sufficient for the experiment.

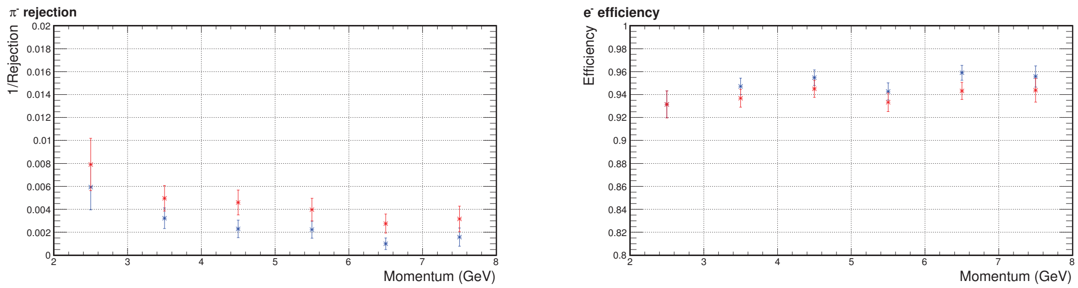

(a) SIDIS large-angle calorimeter

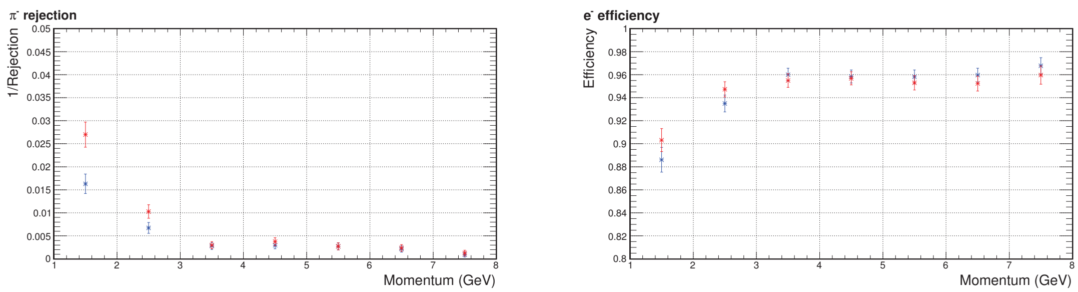

(b) SIDIS forward calorimeter

Figure 97: Calorimeter pion and electron efficiency without (blue) and with (red) the consideration of background particles for the SIDIS configuration. Results for the inner radius region are shown here to provide the worst-case scenario.

In the PVDIS configuration, the background rate is significantly higher and the performance is affected. The 30-fold structure of the baffle system for the PVDIS experiment causes the background to alternate between high- and low-rate 30 times in the azimuthal direction. Therefore, calorimeter performance is studied for the high- and the low-rate "slices" separately, with each fan-shaped slice covering 6 degrees. Background structure for the inner-radius, high-rate slice is shown in Fig. 98. The PID performance with the background is evaluated for different radius, see Fig. 99. Comparing to the intrinsic performance of Fig. 96, the pion rejection is up to 8 times worse. Particle identification for the experiment will need to rely on a full-waveform analysis of the EC, combined with information from the Cherenkov detector.

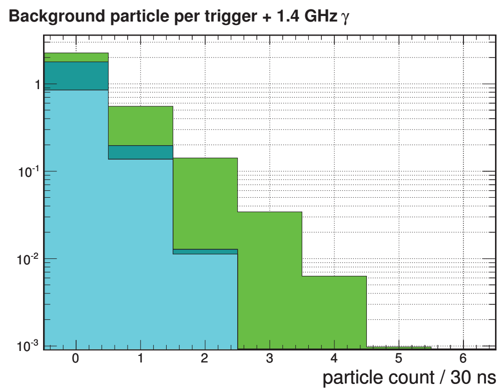

(a) Stacked probability to find the number of background π^- (light blue), π^+ (dark blue) and electrons (green) at the front of the preshower. The photon rate is as high as ~ 1.4 GHz, thus the photon count is off-scale and not shown in this figure.

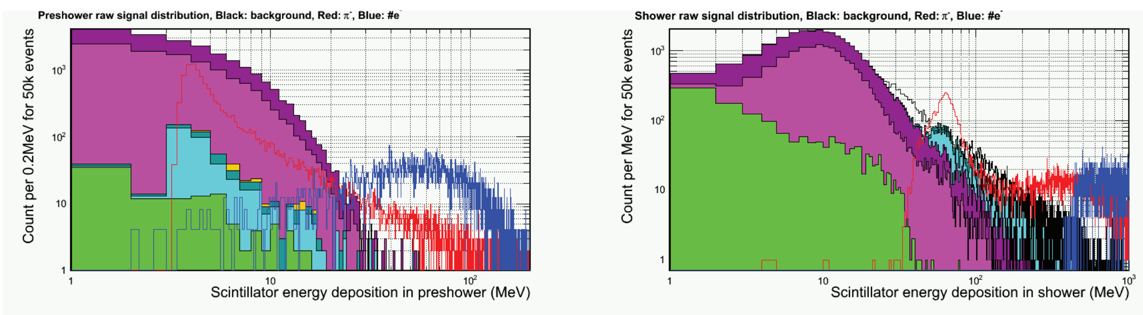

(b) Stacked probability (count per 50k events) vs. Preshower (left) and Shower (right) scintillator energy deposition for incoming background electrons (green), π^- (light blue), π^+ (dark blue), protons (yellow), EM process-originated photons (magenta) and π^0-originated photons (dark magenta). For comparisons, energy deposition for high energy pion (red) and electrons (blue) are shown as non-filled curves.

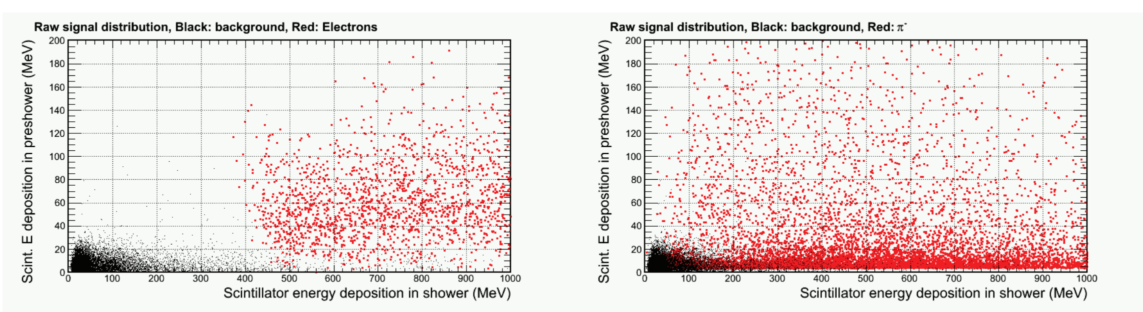

(c) Preshower-shower scintillator energy correlation for background particles (black), compared with high energy electrons (left, red) and pions (right, red)

Figure 98: Background distribution for the PVDIS forward calorimeter at the production luminosity of a liquid deuteron target. Background for the inner radius ($R \sim 1.2$ m) and higher-radiation azimuthal region is shown. The energy deposition originated from background is compatible to that of high energy pions.

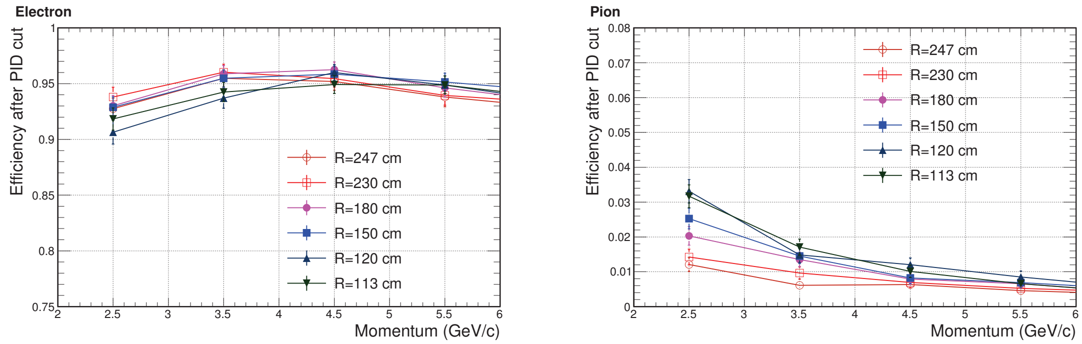

(a) lower-radiation azimuthal region

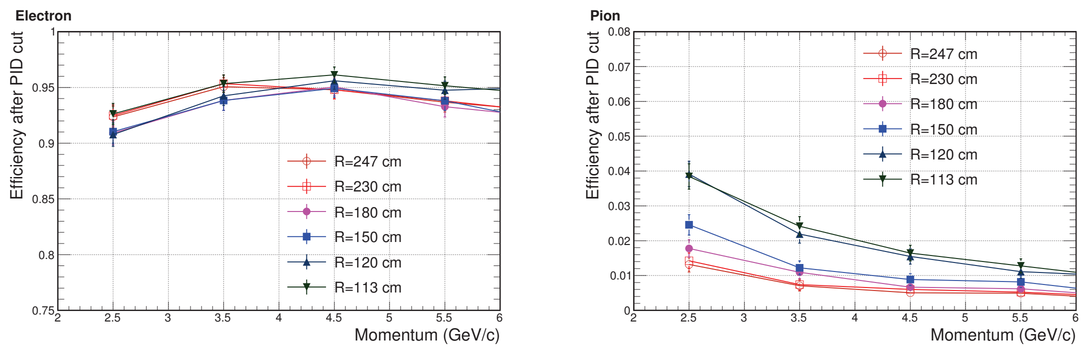

(b) higher-radiation azimuthal region

Figure 99: Calorimeter pion and electron efficiency for the PVDIS experiment, evaluated with the presence of background at eight typical regions on the calorimeter.

10.7.3 Trigger capability

Trigger capability is an important function of the EC. The calorimeter shower energy deposition in all combinations of local 6+1 clusters (central block plus six neighboring hexagon blocks) are first summed after digitization, forming local shower sums. Triggers are then formed by passing the local shower sums through a threshold cut. Electron triggers are formed with a targeted electron threshold, and the efficiency curves for both pions and electrons are studied with the full-background simulation. The following triggering specifications have been studied:

- SIDIS large angle calorimeter: 3 GeV-electron triggers are formed by cutting on local shower sum larger than 2.6 GeV. The trigger turn-on curve is shown in Fig. 100. High electron efficiency is observed for electrons above the threshold. The rejection on few-GeV pion background is high, in the range (20-100):1, which satisfies requirement of the SIDIS experiments.

- SIDIS forward calorimeter: 1 GeV-electron triggers provide high trigger efficiency for electrons. Since the trigger threshold is only about three times higher than the MIP, it leads to a moderate pion rejections as shown on the left plot of Fig. 101. Cherenkov detector will be used in combination to reduce the overall trigger rate in this region.

- SIDIS forward calorimeter: MIP triggers allow the calorimeter to trigger on hadrons for the SIDIS measurement. The threshold is determined by MIP peak - two sigma of the Landau fit of the distribution, which lead to a calibrated local shower sum energy of 220 MeV. The trigger efficiency for pions is high, as shown on the right plot of Fig. 101. To bring the trigger rate ($\sim$20 MHz) down to below the DAQ rate limit, local coincidence signals will be formed between the calorimeter and a scintillator pad detector (SPD). The SPD suppresses the dominant triggering photons by a factor of five, see Section 10.9.

- PVDIS forward calorimeter: electron triggers are formed with radius-dependent trigger thresholds. As shown in Fig. 102, the targeted electron threshold varies from 1.5 GeV at outer radius to 3.8 GeV at inner radius on the calorimeter, which produces high trigger efficiency for DIS electrons with $x > 0.35$. The trigger turn-on curves are evaluated for several regions on the calorimeter as shown in Fig. 102. The efficiency for both electrons and pions are lower for inner radius regions due to the use of high thresholds for background-suppression.

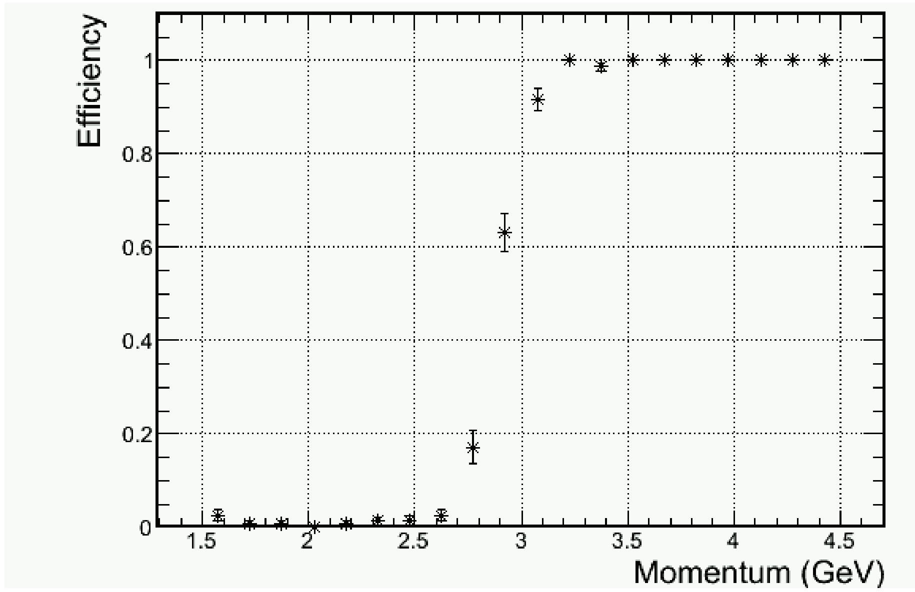

(a) Electron

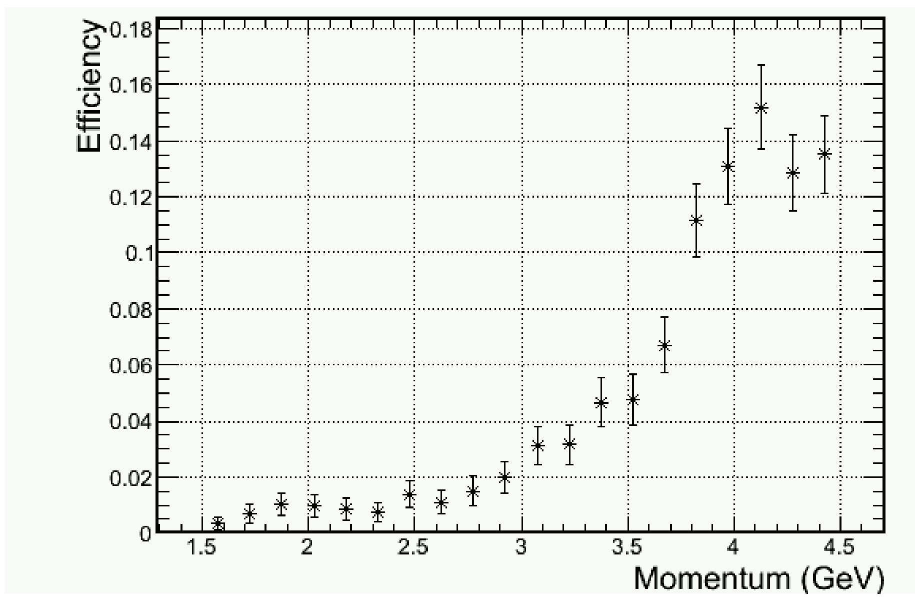

(b) Pion

Figure 100: Trigger efficiency for electrons (a) and pions (b) for the SIDIS large angle calorimeter. The target trigger threshold is approximately $P_e = 3$ GeV$/c$. Only the (high-background) inner-radius region is shown here.

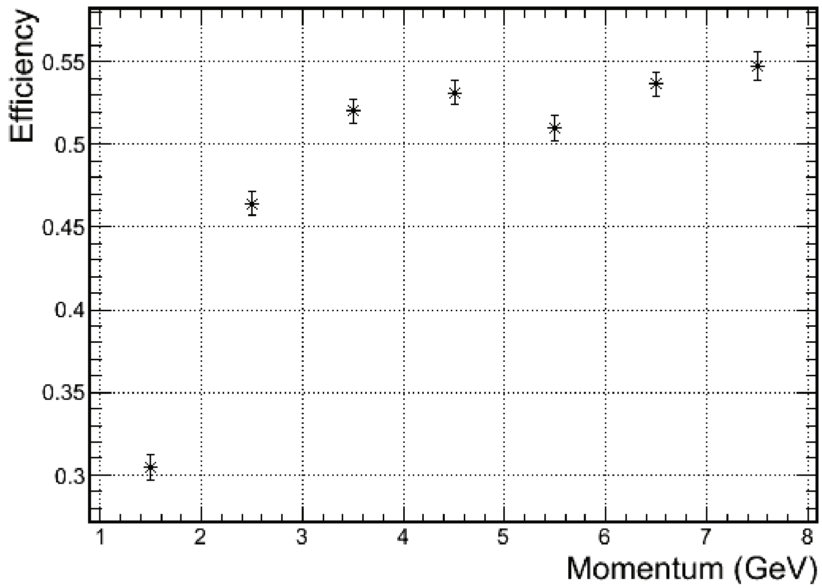

(a) Pion efficiency in electron trigger with a target trigger threshold of ($P_e = 1$ GeV$/c$)

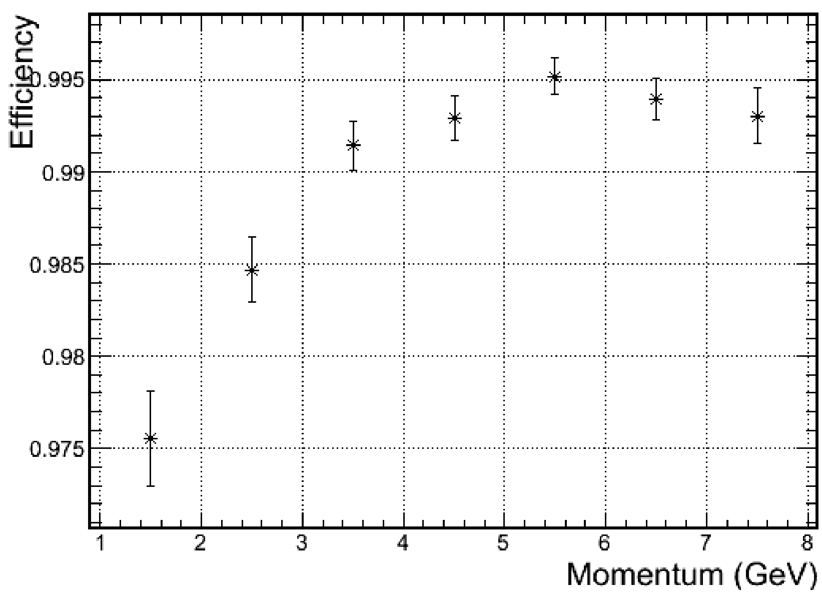

(b) Pion efficiency in the MIP trigger

Figure 101: Trigger efficiency for pions in the SIDIS forward calorimeter for electron triggers (a) and MIP triggers (b). Only the (high-background) inner-radius region is shown here.

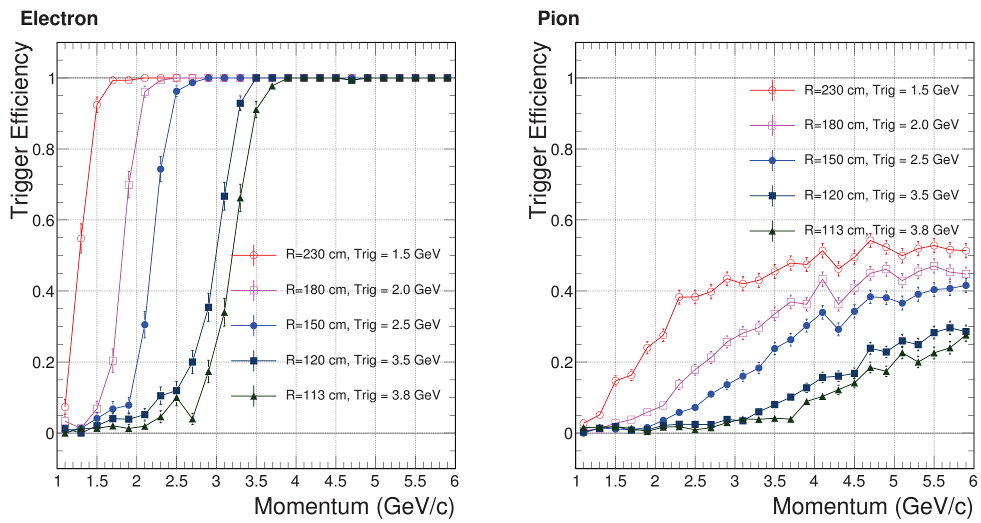

(a) Higher-radiation azimuthal region

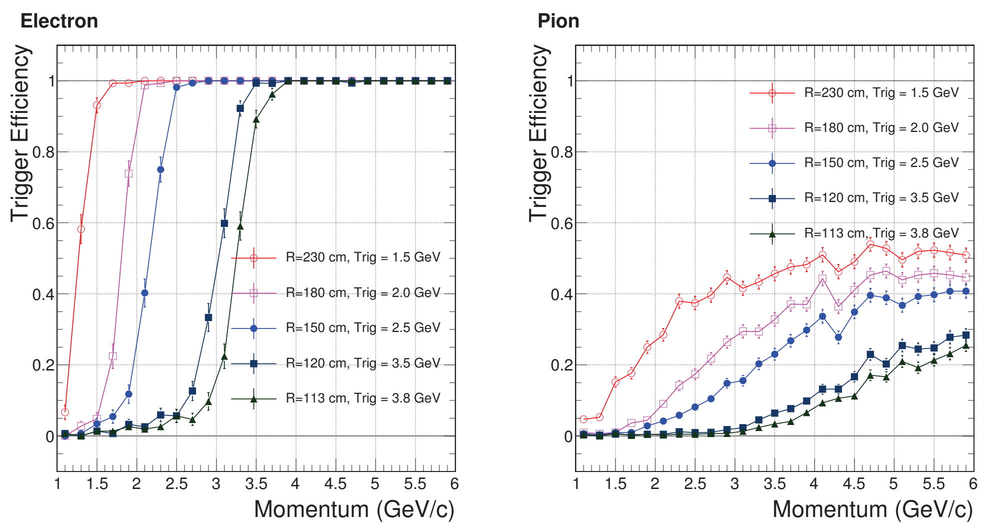

(b) Lower-radiation azimuthal region

Figure 102: Trigger efficiency curves for the PVDIS configuration.

10.7.4 EC trigger rate

The PVDIS experiment will run with a luminosity up to 10^{39} cm^{-2}s^{-1} and thus has high background rates. The trigger of PVDIS will be formed by taking the coincidence between the EC and the gas Cherenkov detector, and care must be taken to ensure the trigger rate is comfortably below the DAQ rate limit. The baffle system is used primarily to reduce the overall rate. To further reduce the rate from high energy photons from neutron pions and low energy backgrounds, fan-shape lead blocks, each covering 2.5 degrees azimuthally, will be placed in front of the EC. As mentioned previously, the EC trigger threshold varies with the radius and is set to preserve DIS electrons with $x > 0.35$. Estimation of the trigger rate is based on the realistic background simulation (described previously in Section 10.7.2). Triggers from low energy backgrounds of $p < 1$ GeV are simulated directly such that background pileups are properly accounted for. For particles with $p > 1$ GeV, pileups are no longer dominant and triggers from these particles are calculated by combining the various particle rates with the trigger turn-on curve. The latter method greatly reduce the simulation time. Table 11 shows the rates of 11 GeV 50 uA electron beams on 40 cm deuterium for each particle type that enter the whole EC and the resulting trigger rates. These results will be combined with gas Cherenkov trigger rate to obtain the expected DAQ trigger rates.

region	full	high	low
rate entering the EC (kHz)			
e^-	413	148	265
π^-	5.1×10^5	2.7×10^5	2.4×10^5
π^+	2.1×10^5	1.0×10^5	1.2×10^5
$\gamma(\pi^0)$	8.4×10^7	4.2×10^7	4.3×10^7
p	5.5×10^4	2.4×10^4	3.1×10^4
sum	8.5×10^7	4.2×10^7	4.3×10^7
trigger rate for $p > 1$ GeV (kHz)			
e^-	321	80	231
π^-	4.8×10^3	3.4×10^3	1.4×10^3
π^+	0.28×10^3	0.11×10^3	0.17×10^3
$\gamma(\pi^0)$	4	4	0
p	0.18×10^3	0.10×10^3	0.08×10^3
sum	5.6×10^3	3.7×10^3	1.9×10^3
trigger rate for $p < 1$ GeV (kHz)			
sum	$(3.1 \pm 0.7) \times 10^3$	$(1.6 \pm 0.4) \times 10^3$	$(1.5 \pm 0.4) \times 10^3$
Total trigger rate (kHz)			
total	$(8.7 \pm 0.7) \times 10^3$	$(5.3 \pm 0.4) \times 10^3$	$(3.4 \pm 0.4) \times 10^3$

Table 11: PVDIS rates that enter full coverage of the EC, and the resulting trigger rates broken down to $p < 1$ GeV and $p > 1$ GeV particles and the low and the high background regions. Here the low and the high-background regions refer to the two 6-degree azimuthal regions of each sector and the azimuthal variation in the background rate is due to the baffle structure. For particles with momentum $p > 1$ GeV, pileup effects are not significant and the trigger rates are obtained by combining the particle entrance rate with the trigger turn-on curves. For particles with $p < 1$ GeV, pileup effects dominate. This requires a timing simulation which is statistically-limited, and is not possible to be broken down to particle types due to the fact that triggers can be produced by different particles piling up on each other. All rates shown are the sum of 30 sectors, divided by 30 to obtain the per-sector rates.

The SIDIS experiment on ^{3}He will run with a luminosity up to 3^{36} cm^{-2}s^{-1} on ^{3}He target and additional about 3.7^{36} cm^{-2}s^{-1} on target glass windows. Both FAEC and LAEC will provide the basic electron trigger. FAEC will also provide MIP trigger for hadron detection.

The FAEC trigger threshold varies with the radius and is set to preserve DIS electrons with $Q^2 > 1$. Estimation of the trigger rate is based on the realistic background simulation including target collimators (described previously in Section 10.7.2) and shown in Table 12 The trigger from EC will be combined with Cherenkov, MRPC and SPD to form the final trigger for SIDIS.

region	FAEC	LAEC
rate entering the EC (kHz)		
e^-	137	18.7
π^-	7.24×10^3	1.55×10^4
π^+	8.08×10^3	1.66×10^4
$\gamma(\pi^0)$	1.76×10^5	2.43×10^5
$e(\pi^0)$	8.40×10^3	2.04×10^3
p	2.36×10^3	6.16×10^3
electron trigger rate (kHz)		
e^-	90	4.7
π^-	500	5.16
π^+	548	5.12
$\gamma(\pi^0)$	1172	16.8
$e(\pi^0)$	81	0.32
p	109	2.15
sum	2500	34.25
MIP trigger rate (kHz)		
e^-	137	
π^-	7080	
π^+	7880	
$\gamma(\pi^0)$	8440	
$e(\pi^0)$	1000	
p	2164	
sum	2.67×10^4	

Table 12: SIDIS ^{3}He rates that enter full coverage of the FAEC and LAEC, and the resulting electron and MIP trigger rates.

10.7.5 Shower Position Measurement

Position resolution of the Shower center was studied for different lateral sizes of the calorimeter modules, as shown in Fig. 103. The radial resolution is in general worse than the azimuthal resolution because the tracks are not perpendicular to the radial direction. As can be seen from Fig. 103, with the use of proper algorithm, a position resolution of better than 1 cm is achieved for both directions at the designed lateral granularity of 100 cm^2.

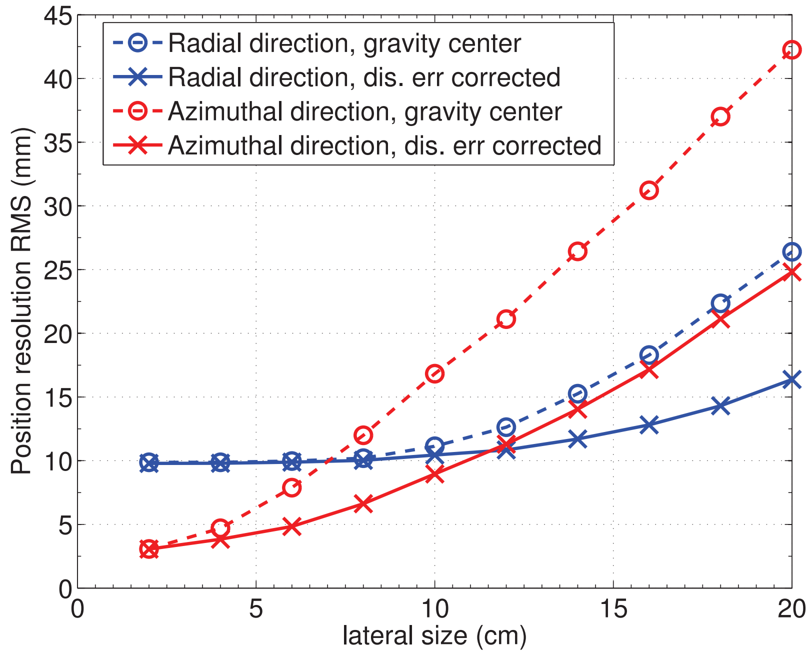

Figure 103: Position resolution for electron showers vs. different lateral size of the calorimeter module. Both azimuthal (red) and radial (blue) resolutions are shown, with the shower center calculated from a simple energy-weighted geometrical center (dashed curves), and those calculated with further corrections using the energy deposition distribution among neighboring modules (solid curves).

10.8 Supplemental Information: PID Selection Cuts

A three dimensional PID cut was used to select the best electron samples with maximal π^- rejection as illustrated in Fig. 104. For each given momentum bin, the cut on E/P and preshower energy roughly follows the contour lines of the ratio of π^- efficiency to e^- efficiency, which is the optimal cut for the π^-/e^- separation. A momentum dependence is then introduced to the cut to maintain a constant 95% electron efficiency for most of the bins. Events passing the cut are highlighted in red in the plots.

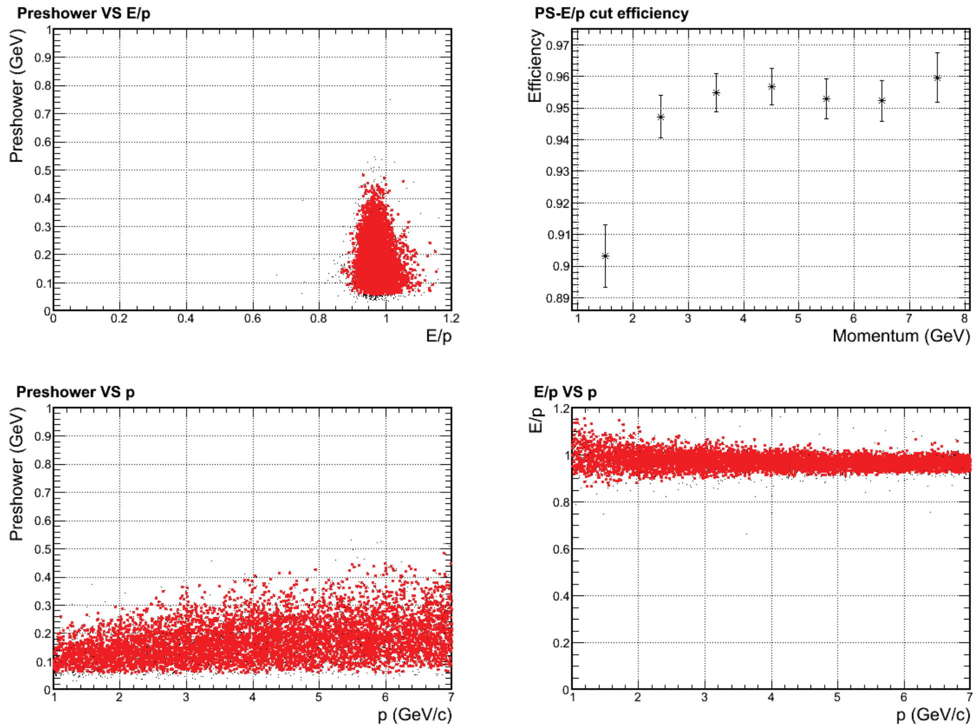

(a)

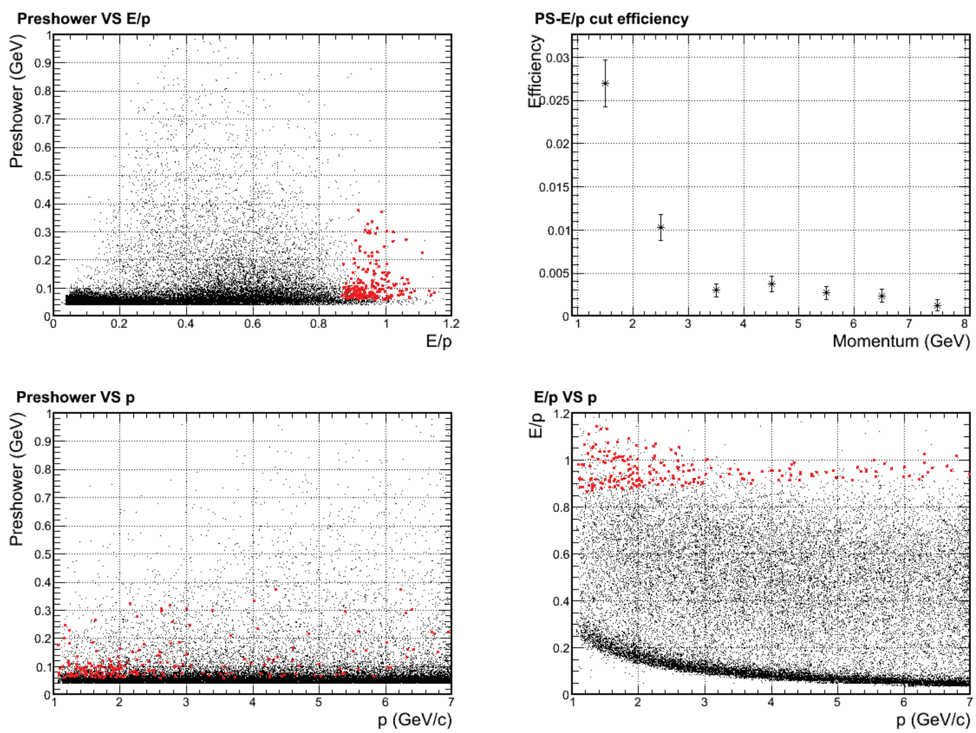

(b)

Figure 104: Illustration of electron sample cuts as highlighted in red dots, in comparison to simulated electron (a) and π^- (b) samples. The SIDIS forward calorimeter in the high background (small radius) region is studied in these plots.

10.9 Scintillator Pad Detector for SIDIS Experiments

The main purpose of the scintillator pad detector (SPD) is to reduce calorimeter-based trigger rates for high-energy charged particles (see Section 10.7.3 for calorimeter trigger capability) by rejecting photons through the coincidence between the SPD and the calorimeter. The SPD consists of fan-shaped scintillator pads arranged perpendicular to the beam direction. Two SPDs will be used: one in the forward direction between the heavy gas Cherenkov detector and the MRPC, and the other in the large-angle direction immediately before the large-angle calorimeter. Photons generated in the scintillator are carried by WLS fibers out of the detector, which are then connected to clear fibers for readout by PMTs. This readout method is similar to that of the calorimeter.

The performance for the scintillator was studied in the GEANT4 simulation and its parameters are optimized to the following:

- We plan to use 3-5 mm thickness scintillator based on a balance between the number of photons to readout and the radiation length. This results in a radiation length of $\sim 1.3\% \times X_0$ which directly affect the photon conversion rate. Typical responses of the SPD to photons and charged particles are shown in Fig. 105. Approximately 20% of the photon background leave energy in the scintillator due to back splashing from the calorimeter front face. This effect is reduced for low energy photon background, which leads to higher rejection as shown in Fig. 106.
- The trigger threshold was set at two standard deviations below the MIP peak to ensure a high efficiency for charged particles.
- Pile up effects were studied by considering a conservative ADC timing window of 50 ns. The photon rejection therefore depends on the trigger rate per scintillator, and further the scintillator segmentation. The segmentation is chosen to balance the consideration of minimizing the number of readout channels, and reducing pile-ups that affect photon rejections.

The segmentation for the scintillator is different for the forward and the large angle region. Since low energy photons dominate the trigger rate, the rejection factors in Fig. 106 are used to optimize the number of segmentation. The results are as follows:

- Large-angle SPD: A 10:1 photon rejection will bring the photon-induced calorimeter trigger rate down to below the electron-induced rate. The 10:1 rejection can be achieved by 60 azimuthal segments, with each segment covering 6 degrees.
- Forward SPD: 60 azimuthal and 4 radial segmentation will be necessary to provide a 5:1 photon rejection. This leads to a sub-dominant fake photon trigger rate in the SIDIS forward MIP and electron triggers. The azimuthal coverage of each SPD segment is 6 degrees and the radial coverages are increased from inner to outer pads, based on equal-rate considerations.

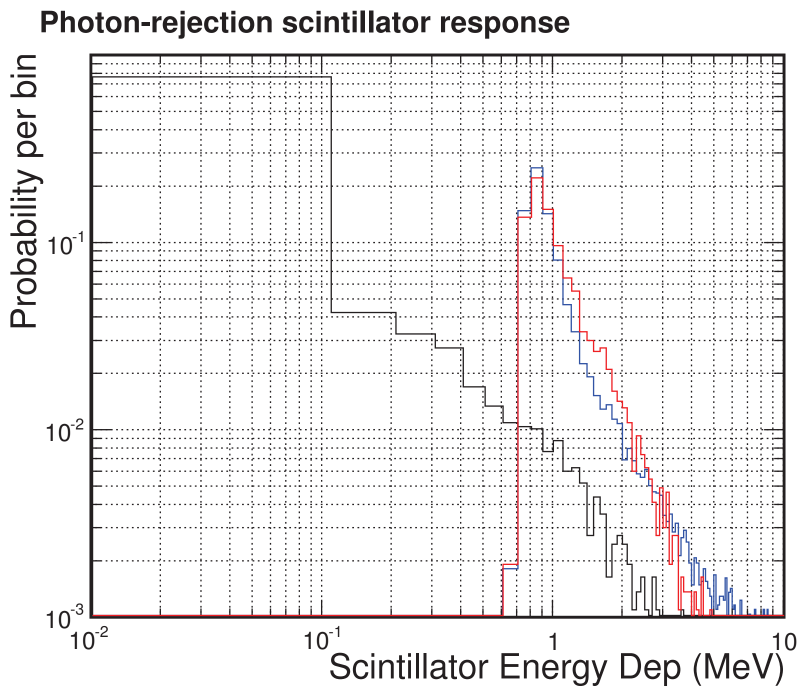

Figure 105: Typical probability for scintillator energy depositions in the SPD, for electron (blue), pion (red) and high energy photons (black).

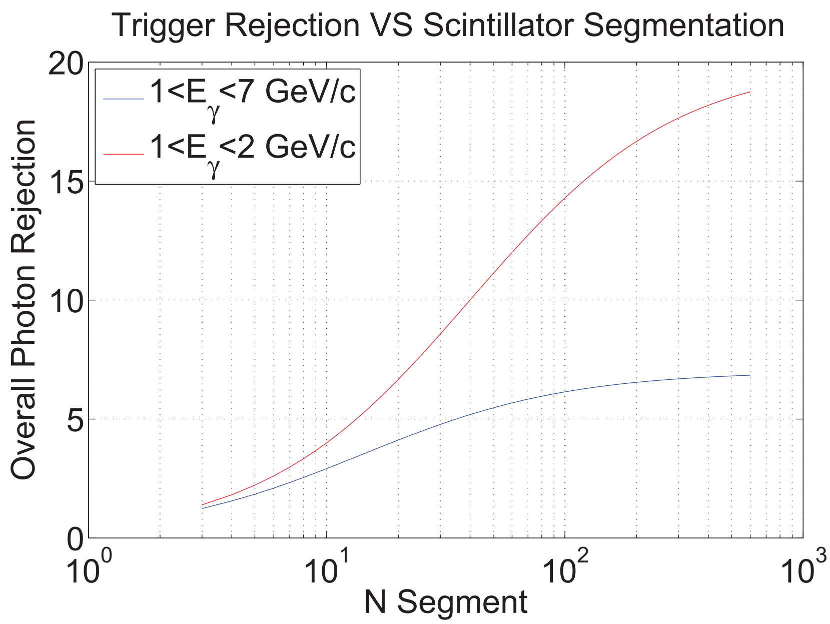

(a) SIDIS large-angle SPD

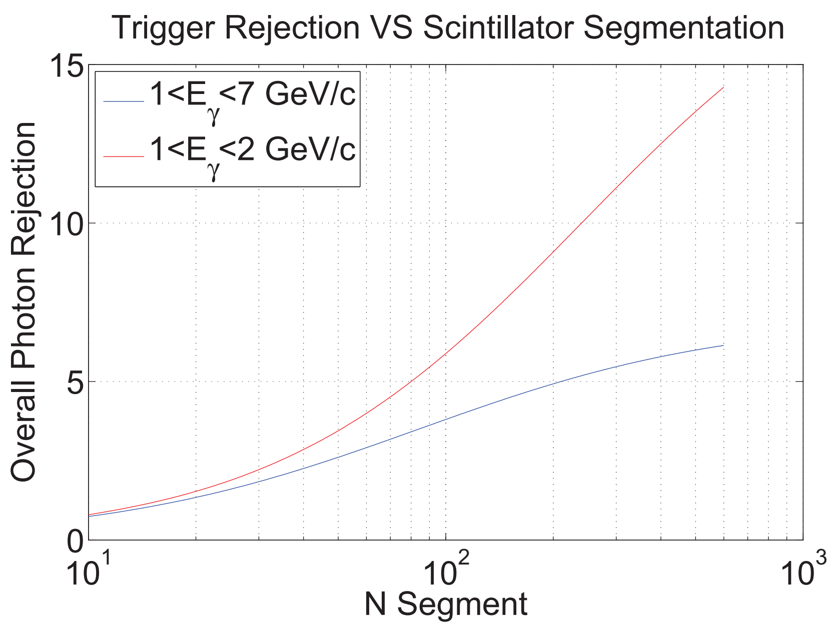

(b) SIDIS forward-angle SPD

Figure 106: SPD high energy photon rejection vs. number of equal-rate segmentation. Two photon energy range were considered: $1 < E_\gamma < 2$ GeV (red curves) and $1 < E_\gamma < 7$ GeV (blue curves). A conservative 50 ns timing window was assumed for calculating the pile up effects.

References

[1] G. Atoian, G. Britvich, S. Chernichenko, S. Dhawan, V. Issakov, et al., Nucl.Instrum.Meth. **A584**, 291 (2008), 0709.4514.

[2] H. Avakian, N. Bianchi, G. Capitani, E. De Sanctis, P. Di Nezza, et al., Nucl.Instrum.Meth. **A417**, 69 (1998), hep-ex/9810004.

[3] E. P. Olloqui (LHCb Collaboration), J. Phys. Conf. Ser. **160**, 012046 (2009).

[4] Y. Kharlov et al., Nucl. Instrum. Meth. **A606**, 432 (2009), 0809.3671.

[5] D. Morozov et al., J. Phys. Conf. Ser. **160**, 012021 (2009).